J. Fluid Mech. (1995), *vol.* 295, *pp.* 357–379

Natural convection in a side-heated cavity: visualization of the initial flow features

By WOLFGANG SCHÖPF AND JOHN C. PATTERSON

Centre for Water Research, University of Western Australia, Nedlands WA 6009, Australia

(Received 17 October 1994 and in revised form 14 February 1995)

The shadowgraph technique is used for visualizing the early stages of the flow in a water-filled square cavity which is suddenly heated and cooled on the opposing sidewalls. These sidewalls are perfect heat conductors, while the top and bottom boundaries of the cavity are thermally insulating. For the first time, a clear visualization is given of the first group of waves travelling up the hot boundary layer immediately after start-up, of the initial horizontal intrusions and of the second group of waves resulting from the interaction of the incoming intrusion with the boundary layer. The properties of the waves are examined and shown to be in agreement with previous numerical predictions. Special attention is paid to the initial horizontal intrusions, and their connection to gravity currents is discussed. One feature in particular which makes these intrusions unique is the interaction with the first group of waves coming from the vertical boundary layers. This interaction together with what appears to be a thermal instability of the intrusion nose are discussed in detail.

1. Introduction

The flow induced in a rectangular cavity with differentially heated and cooled sidewalls is one of the classical heat and mass transfer problems with significance for fundamental fluid mechanics as well as for engineering and geophysical applications. Applications include industrial cooling systems, crystal growth procedures, building insulation, and buoyancy-induced horizontal mass transfer in geophysical flows, to name but a few. Consequently, considerable attention has been paid to this problem in recent decades, with most of the studies focusing on the transient start-up flow following the sudden heating and cooling of the sidewalls; or the stationary laminar flow; or the transition from laminar to time-dependent flow and the route to chaos.

Each of these broad areas of research has a wide literature, but most of the comparatively modern work has focused on the first and last topics. The transition to a time-dependent flow has opened up an interest in the stability of the laminar flow, and is expected to describe some of the aspects of the transition of a thermally driven flow to turbulence. These transitions strongly influence the heat-transfer characteristics and are therefore of considerable engineering interest. Most of the work in this area has been numerical, in the sense that full, usually two-dimensional, numerical solutions of the equations of motion are obtained for a particular value of the Rayleigh number, which is then slightly increased and the stability of the solution is observed. Papers by Le Quéré & Penot (1987), Paolucci & Chenoweth (1989), Henkes & Hoogendoorn (1990), Le Quéré (1990*a*, *b*) and Janssen, Henkes & Hoogendoorn (1993) are representative of this approach. Evidently the only

experimental observation of the transition from the laminar cavity flow to a time-dependent state is that of Briggs & Jones (1985).

The study of the transient flow immediately following the initiation of heating and cooling on the opposing sidewalls (in the following also called the *start-up*) has also only a relatively recent history, with the first discussion of the flow by Patterson & Imberger (1980). Subsequent papers by, for example, Yewell, Poulikakos & Bejan (1982), Ivey (1984), Schladow, Patterson & Street (1989), Schladow (1990) and Patterson & Armfield (1990) all addressed various aspects of this problem, including both experimental and numerical observations. In many of the geophysical and industrial applications, the imposition of the horizontal temperature gradient is time dependent and therefore an understanding of the temporal development of the flow and of the heat transfer properties is an important issue, particularly if the resulting flow is chaotic.

The specific problem of interest here is that of a rectangular cavity which contains an initially isothermal and motionless fluid. The flow is started by instantaneously raising and lowering the temperatures of the opposing sidewalls by the same amount, and then maintaining those temperatures. The evolving flow consists of narrow vertical boundary layers adjacent to the heated and cooled walls, which exit into horizontal intrusions travelling across the roof and floor of the cavity before meeting with the opposing wall boundary layers. The complex interaction between the incoming intrusion and the receiving boundary layer establishes the means by which the core region of the cavity stratifies. For a sufficiently low Rayleigh number, a laminar time-independent flow is achieved by the adjustment of the core flow, the intrusions and the boundary layers. At a higher Rayleigh number, however, a time-periodic flow may result, or if the Rayleigh number is sufficiently high, the flow becomes turbulent. The route to a time-dependent flow depends on the aspect ratio of the cavity, the Prandtl number of the fluid and the thermal boundary conditions.

Although there are many phases to the development of the flow from the motionless isothermal condition to one characterized by a variety of length and velocity scales, one sequence of events in the early part of the flow is particularly striking. This is the presence of two separate groups of short-lived travelling waves observed on both the vertical boundary layers and the intrusion flows. The first group of waves follows start-up and the second one emerges from the first interaction between the incoming intrusion and the opposing boundary layer. The presence of these waves was identified from experimental and numerical observations (Patterson & Armfield 1990; Schladow 1990). Schladow (1990) suggested that the first group of waves was similar to the one observed when a semi-infinite plate is suddenly heated (see for example Ingham 1985; Joshi & Gebhart 1987). Armfield & Patterson (1992) used a linear stability analysis of the numerically computed solutions for the boundary-layer part of the flow to calculate the maximally amplified and fastest moving components of the first group of waves. These predictions were shown to match the properties of the observed waves. The same authors also proposed that the so-called leading-edge effect, the means by which the developing boundary layer begins its transition to a stationary flow, was in fact the group of waves initiated at the leading edge (the upstream corner of the cavity). The transition occurs as the fastest moving wave component travels along the transient boundary layer. This resolved the paradox of previous models, which assumed that the leading-edge signal was advected along the layer by the much slower mean flow (Goldstein & Briggs 1964; Brown & Riley 1973). These models predicted speeds of the leading-edge effect which were significantly lower than those observed.

Also of considerable interest is the horizontal intrusion flow. There has been an extensive discussion on the nature of the complex diverging flow formed near the exit from the vertical boundary layer into the horizontal intrusion after the flow has become established. Some authors (Ivey 1984; Paolucci & Chenoweth 1989) suggested that the flow was due to an internal hydraulic jump, while others took the view that the rapid divergence in the flow and the formation of recirculating zones against the wall resulted from other effects. These include the concentration of vorticity in the region of the intrusion discharge (Schladow *et al.* 1989), blocking effects induced by the changing thermal boundary conditions (Patterson & Armfield 1990), and the detachment of the fluid from the ceiling like a plume at high Rayleigh numbers (Ravi, Henkes & Hoogendoorn 1994). Whatever the processes governing the flow are, the observations indicate a complex interaction of the first intrusion following the start-up with the first group of waves coming from the vertical boundary layer, and also of the intrusion with the far-wall boundary layer.

The heat-transfer properties of the cavity during the initial start-up are controlled by the development and subsequent behaviour of the thermal boundary layers, which serve to transport the heat into and out of the cavity core, and of the intrusion flows, which advect the heat across the cavity. Numerical calculations clearly show the presence of oscillations in the heat-transfer rate across the cavity due to the travelling-wave groups interacting with the intrusion flows (see e.g. Patterson & Armfield 1990; Schladow 1990). Furthermore, the transient flow has the potential to become turbulent, which again leads to important implications for engineering heat-transfer calculations.

In all of the investigations discussed above, there were only indirect experimental confirmations of even the existence of the travelling-wave groups. Patterson & Armfield (1990) and Jeeveraj & Patterson (1992) showed evidence of the waves by isolated temperature measurements using thermistors which were placed inside the vertical boundary layer and in the horizontal intrusion. The visualization technique used by those authors could reveal an overall picture of the large-scale flow field, but the timing for the streak photographs was not appropriate for the relatively fast travelling waves. The experiments by Yewell *et al.* (1982) and Ivey (1984) were not directed at the relatively high-frequency waves observed during the start-up. There appear to be no other experiments focusing on the transient part of the cavity flow.

The main difficulty with the temperature time series taken at one or more fixed locations is that only localized properties can be obtained. As Armfield & Patterson (1992) showed, the properties of the waves alter as they move downstream, and the true character of the wave groups is not revealed unless a very large number of sampling locations is available. In the experiments by Patterson & Armfield (1990) and Jeeveraj & Patterson (1992), however, data were sampled only at one or two sites in the boundary layer, therefore no or only very limited information on wave velocities and wavenumbers was available.

To overcome these problems for the present experiments, the shadowgraph technique is used as a means of flow visualization. Rather than yielding temperature time series only at specific locations, the shadowgraph images give an overall (two-dimensional) map of the temperature signal. Since the heat transport in the early stages of the flow is mainly determined by convective processes, the images are also a very good representation of the flow field. The experimental setup is explained in § 2. A brief description of the apparatus is followed by a discussion of the optical setup and of the use of the shadowgraph method in our experiments. In § 3, we show experimental results from the transient part of the flow immediately following start-up,

including the first and second groups of waves on the vertical boundary layers and the initial intrusions along the horizontal walls. For the first time a clear visualization of these features is given. The results are discussed in detail in §4, which includes a qualitative and, where possible, quantitative comparison with previous experimental and numerical work. Connections to other, different systems showing similar results are also made. In the concluding §5 we include an outlook and motivations for future work.

2. Experimental setup

2.1. *Experimental tank and fluid properties*

The problem being examined here is that of an initially motionless Newtonian fluid, which is contained in a square cavity of dimension h and held at the ambient temperature T_0. The vertical sidewalls are assumed to be perfect heat conductors, while the horizontal upper and lower boundaries are thermally insulating. The transient flow is initiated by suddenly increasing and decreasing the temperatures of the opposing sidewalls by the same amount ΔT, thus changing their values from T_0 to $T_0 + \Delta T$ and $T_0 - \Delta T$, respectively. The resulting flow is assumed to be two-dimensional with the relevant coordinates being x in the horizontal and y in the vertical direction and the origin lying in the lower hot corner. The non-dimensional parameters describing this problem are the Rayleigh number and the Prandtl number:

$$Ra = \frac{g\alpha h^3 \Delta T}{\kappa \nu}, \qquad Pr = \frac{\nu}{\kappa} \tag{2.1a,b}$$

where g is the acceleration due to gravity, h is the height and width of the cavity, α, ν and κ are respectively the coefficient of thermal expansion, the kinematic viscosity and the thermal diffusivity of the fluid, and ΔT is the temperature difference between the sidewalls and the mean temperature T_0. For a rectangular, non-square cavity, another relevant parameter would be the aspect ratio.

The experimental rig is that described by Patterson & Armfield (1990), therefore only a brief description is given. The cavity containing the working fluid is constructed from Perspex in order to both model the insulating boundary conditions and to make the tank transparent to light, except for the conducting sidewalls which are made from copper of thickness 1 mm. The size of the two-dimensional working region is 24 cm × 24 cm and the extent in the third dimension is 50 cm. Adjacent to each copper wall is a large reservoir containing heated or cooled water, which is maintained at the desired temperatures of the hot and cold walls. These reservoirs are separated from the copper walls by removable gates leaving an air gap between the gates and the copper. In order to minimize radiative and convective heat transfer from the water reservoirs to the copper walls, insulating sheets of styrofoam and heat exchangers are attached to the cavity side of the gates. During the setting-up, water at the cavity temperature is circulated through these heat exchangers. On initiation, the gates are raised pneumatically, so that the heated and cooled water floods against the copper walls. The conduction time scale for the heat flow through the thin copper plates is of the order of 10 ms, therefore this procedure provides a very rapid change of the thermal boundary condition. This change is much faster than the time scale for the boundary layer growth, the order of which is given by $h^2/(\kappa Ra^{1/2})$ (Patterson & Imberger 1980) and is about 15 s for our setup. Therefore, the desirable step-change in the thermal boundary condition is very well approximated.

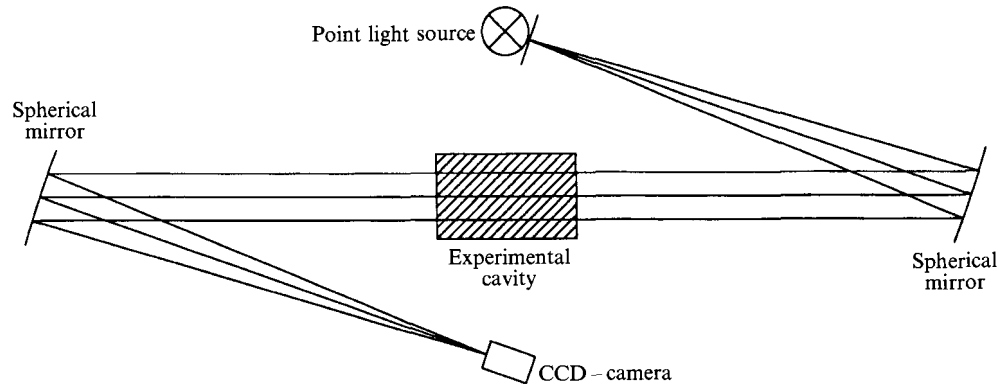

FIGURE 1. Sketch of the optical setup. White light coming from a halogen lamp through a pinhole and made parallel by means of a spherical mirror is transmitted through the cavity, thus illuminating the two-dimensional working region. A second mirror focuses the deflected light on a CCD–camera. The resulting images are stored and further processed using the frame-grabbing facilities implemented in a PC/AT–computer (not shown here).

The experiments reported here have been carried out with water as the working fluid. The mean temperature was $T_0 = 20.40$ °C which gives a Prandtl number of $Pr = 7.0$. The temperatures of the vertical sidewalls were raised and lowered by $\Delta T = 3.5$ K, corresponding to a Rayleigh number of $Ra = 7.2 \times 10^8$.

2.2. *Optical setup and shadowgraph technique*

The optical setup is sketched in figure 1. A point light source is generated by placing a pinhole in front of a halogen lamp. The light is made parallel by means of a spherical mirror, which has a diameter of 30 cm and a focal length of about 2.4 m. The resulting parallel light beam shines through the experimental tank in such a way that the two-dimensional working region is illuminated. A second mirror, which is identical to the first one, converges the transmitted light at a CCD–camera, leading to the Z-shaped setup shown in figure 1.

Visualization of the temperature field is achieved by the well-known *shadowgraph* technique (see for example Busse & Whitehead 1971; Merzkirch 1974). This inexpensive, easy-to-handle but extremely sensitive method has proven very successful for application in fluid flows involving thermal gradients. The principles are rather simple: the temperature variations with space and/or time inside the fluid lead to a spatial and/or temporal modulation of the refractive index of the fluid, which in turn leads to space- and/or time-dependent deflections of the incoming parallel light beam. Therefore, the distribution of the light intensity in the shadowgraph image is a representation of the spatial temperature field inside the fluid, while a time series of images can reveal its temporal evolution.

Recently, this method has been used for quantitative measurements of the temperature variations in different experiments relating to Rayleigh–Bénard convection (Rasenat *et al.* 1989; Winkler & Kolodner 1992; Schöpf & Rehberg 1994). This, however, was only possible because the angle of deflection from the direction of the parallel light was very small, which had been achieved either by using a very narrow apparatus or by working very close to the convection onset where temperature modulations are small, or both.

These prerequisites are not met in our experiment. The cavity is relatively long (more than twice the lateral dimension), and the temperature gradients are in general not small (their order is given by the ratio of the applied temperature difference ΔT to the thickness of the boundary layer). Therefore, we cannot expect to obtain a quantitative temperature measurement by this technique in our case. On the other hand, the shadowgraph images are still extremely good qualitative representations of the temperature field and yield a very high quality of flow visualization (see figure 2 below). Roughly speaking, this visualization method is most sensitive to changes in the second derivative of the refractive index (Merzkirch 1974), and therefore those maximal changes lead to the strongest contrasts in the shadowgraph images. By following such bright and dark spots in space and time, it is easily possible to determine for example the speed or wavelength of moving patterns. The quantitative intensity distribution on the image, however, depends in a strongly nonlinear way on the variation of the refractive index (for details see Merzkirch 1974 and Rasenat *et al.* 1989).

If the heat transport is mainly by convection rather than by conduction (as is the case here) the shadowgraph images are also a very good representation of the velocity field in the fluid. In this case, the technique virtually acts as a tracer method. However, the strong focalization by the temperature gradients may lead to caustics in the images (see the extremely bright features in figures 2–6). Therefore, the apparent location of such a feature on the shadowgraph image may not be identical to its actual location inside the cavity. This error can be estimated by the overlap of the feature under consideration (e.g. the intrusion nose) with an object of known dimension which has been introduced into the cavity (e.g. the stirrer as described in § 2.3 and shown in figure 2). From several such experiments, we found that the maximal error, which occurs only for the strongest temperature signals, is about 2 mm.

2.3. *Frame-grabbing procedure*

The black-and-white CCD–camera is connected to a frame-grabber board which is implemented in a PC/AT–80486 computer. The board digitizes the shadowgraph images received by the camera into an array of 512×512 pixels of 8-bit grey-scale values. The pictures are stored on the hard disk of the computer and can be further processed later. With our combination of equipment, we were able to take and store one full image every 2.44 s. The procedure was the following: between starting the frame-grabbing program and initiating the flow by raising the gates, we waited a few seconds in order to take some images before start-up and not miss out on important stages of the flow. The first image *after* start-up was taken about 2 s after releasing the gates. Since the start-up is initiated manually, a slight error of the order of 0.5 s is introduced into the absolute timing. This error, however, is exactly the same for all images and has no influence on the relative timing. The time elapsed between two consecutive pictures is always 2.44 s, the error of which is given by the quartz oscillator of the CCD-camera and is therefore negligible. Having this in mind, *all* times are given to hundredths of a second in the following.

The diameter of the spherical mirrors (30 cm) is smaller than the diagonal dimension of the two-dimensional working region (34 cm), therefore we cannot display the whole region of interest. As a result, only little more than one half of the cavity is shown, which is always the heated half. In principle, the problem is completely symmetric, although in practice non-Boussinesq effects and small differences in the timing of the release of the gates or in the temperature differences may lead to a slightly asymmetrical situation. Figure 2 shows three examples of the shadowgraph images,

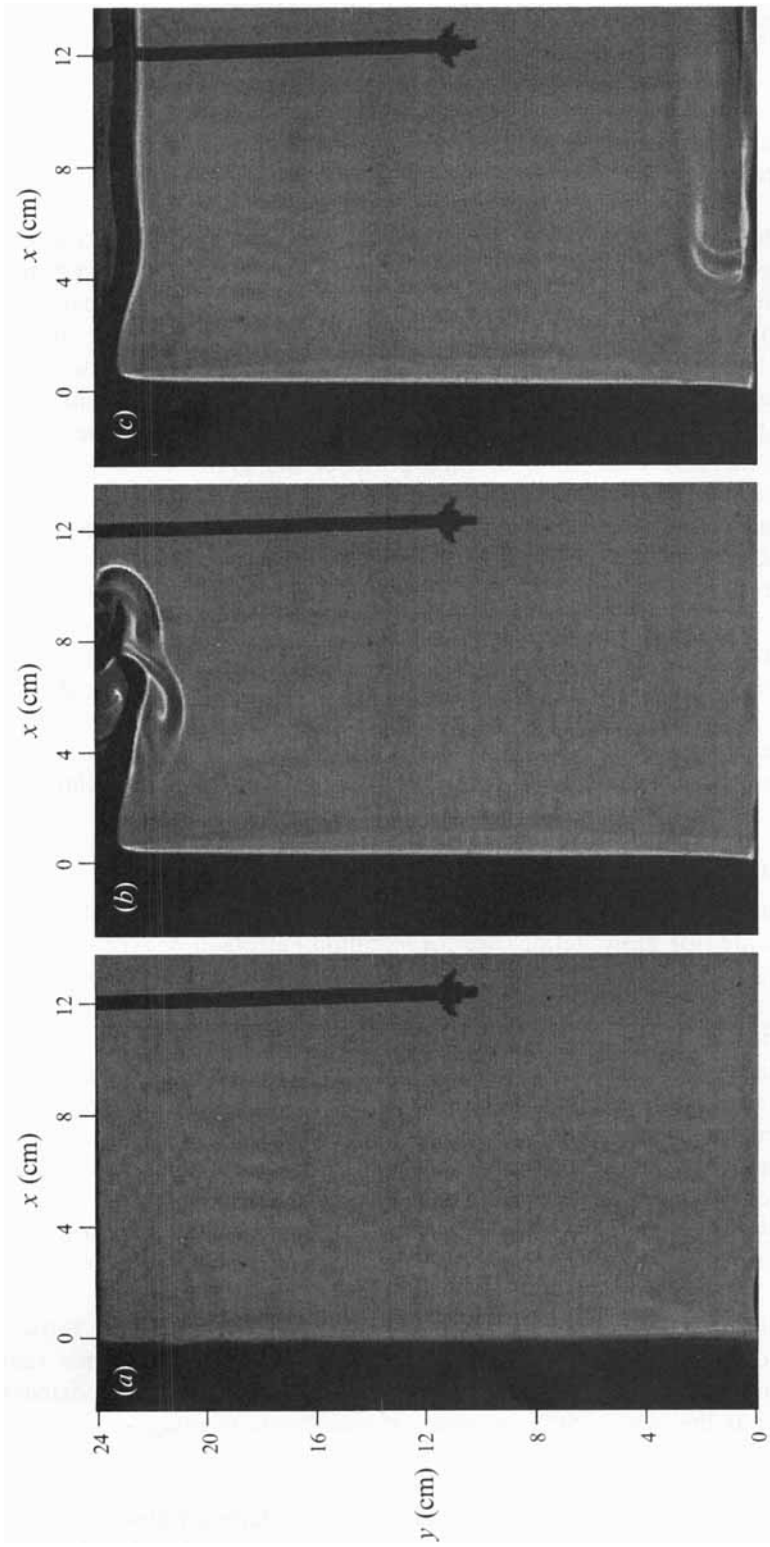

FIGURE 2. Examples of shadowgraph images as used for composing figures 3 to 6 below. Only the heated half of the cavity is shown. The hot wall is to the left and the stirrer visible at the right-hand side of the pictures is placed half-way across the cavity. The labels at the left-hand side and at the top indicate the distances in cm from the bottom and from the hot (left) wall, respectively. (*a*) Motionless and isothermal state before the initiation of the flow. (*b*) 41.04 s after start-up. The hot intrusion exiting from the upper left corner and travelling along the top of the cavity to the right is obvious. (*c*) 70.32 s after start-up. The nose of the hot top intrusion has travelled out of the field of view, leaving a band of laminar flow behind. The incoming cold intrusion can be seen on the floor of the cavity and will soon hit the hot boundary layer. The shape of the boundary layer can be identified from (*b*) and (*c*).

taken at three different instants in time. Figure 2(*a*) is taken prior to applying the temperature difference, thus showing the motionless isothermal base state. The top and bottom boundaries of the cavity coincide with the edges of the picture, and the vertical wall which subsequently will be heated can be seen to the left. The origin for the system of coordinates as used in the remainder of the paper lies in the lower left corner, with x increasing to the right and y upwards (see labels in figure 2 and also in figures 3–6).

The feature visible near the right-hand side of the picture is a small stirrer which has been introduced into the cavity as part of the preparation for each experiment. This allowed a uniform temperature distribution to be obtained much faster than without stirring, in which case the waiting time would be dictated by the diffusion time scale for the temperature gradients. By using the stirrer, however, the waiting time can be reduced to the diffusion time scale for the velocity gradients, which is an improvement from the order of days to the order of hours. The middle of the top part of the rod holding the stirrer indicates the mid-point of the cavity corresponding to $x = 12$ cm. Since the diameter of the rod is only 5 mm, the interference of the stirrer with the flow is minimal, and it is merely a disturbance of the vision of the flow.

Figure 2(*b*) is taken 41.04 s after start-up and shows the initial hot intrusion at the top of the cavity. In figure 2(*c*), which is taken 70.32 s after start-up, this intrusion has already proceeded more than half-way across the cavity, but now the corresponding cold intrusion coming from the far cold wall can be seen on the floor of the cavity. From these pictures the general shape of the vertical boundary layer is identified and the presence of the intrusions on the horizontal boundaries is clear. A detailed visualization and discussion of all these features will be presented in §§ 3 and 4 below. This is the first time that these features have been made visible with such clarity.

3. Observations from the shadowgraph images

Directly after start-up, two different but interacting features are expected to occur on the same time scale (for more details, see for example Patterson & Armfield 1990; Armfield & Patterson 1992). For simplicity and because of the symmetry of the problem, only the processes near the hot wall will be discussed. Firstly, a thermal boundary layer adjacent to the wall is established by thermal conduction. Since the fluid in this boundary layer is warmer and thus lighter than the surrounding fluid, a convective flow up the boundary layer starts simultaneously. At the top corner of the cavity this flow turns from vertical to horizontal and forms the beginning of the hot horizontal intrusion flow. Secondly, the singularity at the lower hot corner acts as a strong disturbance to the unstable boundary layer and triggers a group of waves, which subsequently travel up the boundary layer. This is the so-called leading-edge effect. The waves move faster than the mean flow in the boundary layer and, for a sufficiently high Rayleigh number, are amplified during their journey. They will finally arrive at the top corner of the cavity and exit into the horizontal intrusion flow leading to a complicated series of interactions. These processes are made visible by means of the shadowgraph technique presented above, and will now be discussed in detail by looking at the respective time series of shadowgraph images.

3.1. *First group of travelling waves*

Figure 3 is a visualization of the boundary-layer flow immediately following start-up and shows the initiation of the first group of waves travelling up the hot boundary layer. Each part of the picture shows the same narrow vertical strip ($\approx$ 1.1 cm wide)

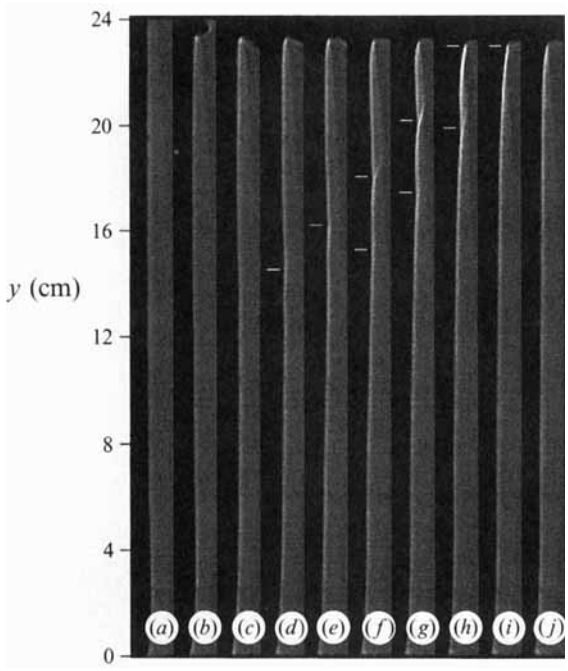

FIGURE 3. Time series of shadowgraph images showing the first group of travelling waves. The labels at the left-hand side indicate the distance in cm from the bottom. Each part of the figure represents the same narrow region ($\approx$ 1.1 cm) of the tank around the hot boundary layer, but is taken at a different instant in time. The individual parts correspond to the following times after start-up: (*a*) 4.44 s, (*b*) 9.32 s, (*c*) 14.20 s, (*d*) 16.64 s, (*e*) 19.08 s, (*f*) 21.52 s, (*g*) 23.96 s, (*h*) 26.40 s, (*i*) 28.84 s, (*j*) 31.28 s. From (*c*) to (*j*) the pictures are equally spaced in time with 2.44 s elapsed between consecutive images. The white markers in (*d–i*) indicate the two distinct peaks visible in the first group of waves which travel up the boundary layer. (*j*) shows no sign of wave motion.

covering the hot boundary layer, and is extracted from a full image similar to those ones presented in figure 2, each one taken at a different instant in time. The hot wall is to the left, the fluid flows from bottom to top and time increases from left to right, i.e. from figure 3(*a*) to (*j*). In each case, the curved dark region at the left which is bounded by a thin bright line corresponds to the inner edge of the boundary layer.

Figure 3(*a*) is taken 4.44 s after initiation of the heating. The thermal boundary layer has already evolved and its shape is clearly visible, growing from the bottom corner. In figure 3(*b*), taken 9.32 s after start-up, the early parts of the horizontal intrusion can be recognized in the top corner. Figure 3(*c*), taken at $t = 14.20$ s, is similar at the upstream end, but with the horizontal intrusion already proceeding further downstream. The subsequent pictures are equally spaced in time, with 2.44 s elapsed between consecutive images, so that figure 3(*d*) corresponds to $t = 16.64$ s and figure 3(*j*) to $t = 31.28$ s. In figure 3(*d*), a wave is visible for the first time at a distance slightly above the mid-height of the cavity, indicated by the white marker. Presumably, it was also present in the first few frames, but was too small in amplitude to be visible. This first peak can be followed through figure 3(*e–g*) until it reaches the downstream corner by figure 3(*h*) and is about to exit into the horizontal intrusion. A second peak in the first group of waves has established a barely visible amplitude in figure 3(*f*) as marked there. It moves downstream through figure 3(*g*, *h*) and into

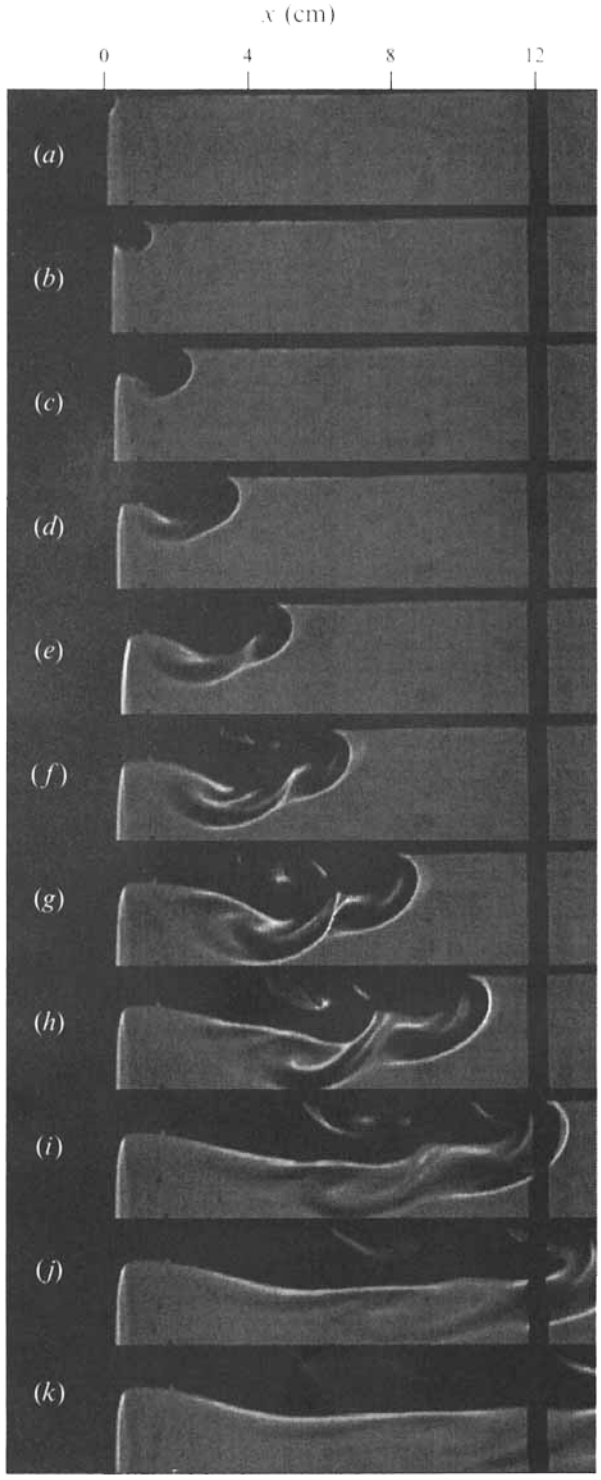

FIGURE 4. For caption see facing page.

the corner in figure 3(*i*), again ready to exit into the horizontal intrusion. In the final figure 3(*j*), all indications of the first group of travelling waves have disappeared.

3.2. *Horizontal intrusions*

The start and progress of the horizontal intrusion along the roof of the cavity are documented in figure 4. Similarly to figure 3, this is again a time series, but now of a horizontal strip ($\approx$ 3.22 cm wide) around the top intrusion. Time proceeds downwards from figure 4(*a–k*) with 4.88 s elapsed between consecutive pictures, so that figure 4(*a*) is taken 6.88 s and figure 4(*k*) 55.68 s after start-up. In this series, the intrusion progresses from being barely visible to being well past the mid-point of the cavity. The top part of the hot boundary layer can be identified to the left.

Initially, the intrusion shows some of the characteristics commonly observed in gravity currents, with a well-defined intrusion head and detraining fluid being left behind as the intrusion proceeds (see for example Britter & Simpson 1978; Simpson & Britter 1979; Simpson 1982), but no mixing at the interface of the head and the ambient fluid is evident. With the no-slip condition at the wall, the foremost point of the intrusion (the *nose*) is some distance away from the wall, as expected. The described properties are clearly evident in figure 4(*a–d*), ranging from $t = 6.88$ to 21.52 s. In figure 4(*e*), however, two new features have appeared. Firstly, a small and initially weak temperature structure, which can be seen approximately half-way between the vertical boundary layer and the intrusion nose, has formed at the intersection of the intrusion with the top wall. Secondly, the nature of the detraining fluid seems to have changed, with the formation of a distinct temperature structure intruding into the head of the intrusion.

These features remain throughout the rest of the time series. In figure 4(*f*), the temperature structure adjacent to the wall has moved downstream and become more intense. It then continues to move slowly (relative to the velocity of the nose) downstream and becomes larger in extent. Its intensity increases until figure 4(*h*) and then decreases again, almost vanishing by figure 4(*k*). This structure appears to be associated with the vertical expansion of the intrusion and indicates the presence of a region of flow separation. The feature near the point of detrainment has also intensified in figure 4(*f*) and two new similar structures have appeared. Further downstream it also weakens, although the regular pattern of temperature modulation is evident in figure 4(*g–i*). By figure 4(*j*), however, it is almost completely gone and seems to have dispersed while travelling downstream. This feature is associated with the arrival of the first group of waves from the hot boundary layer (see discussion in § 4.3).

Another new characteristic has appeared in figure 4(*f*): a bright band inside the head aligned with the nose, corresponding to a temperature maximum. This structure not only remains with the intrusion throughout the rest of the sequence, but also

FIGURE 4. Time series of shadowgraph images showing the hot intrusion. The labels at the top indicate the distance in cm from the hot (left) wall. Each part of the figure represents the same region ($\approx$ 3.22 cm) of the tank around the top boundary, but is taken at a different instant in time with 4.88 s elapsed between consecutive images. The individual parts correspond to the following times after start-up: (*a*) 6.88 s, (*b*) 11.76 s, (*c*) 16.64 s, (*d*) 21.52 s, (*e*) 26.40 s, (*f*) 31.28 s, (*g*) 36.16 s, (*h*) 41.04 s, (*i*) 45.92 s, (*j*) 50.80 s, (*k*) 55.68 s. The progress of the intrusion head and the evolution and decay of several distinct temperature features between the nose and the tail of the intrusion are evident and are discussed in the text.

intensifies. In figure 4(*h*) the band appears to have split and formed a second band, and it also seems that the nose itself is shedding another structure. Owing to the presence of the stirrer and the fact that the intrusion head moves out of the visible region, this last suggestion is not fully evident from this picture but will be supported by the cold intrusion seen in figure 5 and discussed in the next paragraph. These bands of temperature maxima correspond to a wave-like structure being advected along with the intrusion nose.

The nose of the hot intrusion disappears from the field of view in figure 4(*k*), however the corresponding cold intrusion coming from the far wall has entered the visible region. Although the symmetry is not perfect, the main features of the cold intrusion correspond to those of the hot one. Figure 5 shows, in the same form as figure 4, a time series of the progress of the cold intrusion, with each horizontal strip being about 2.46 cm wide. Again, the images are equally spaced in time with 4.88 s elapsed between consecutive pictures. Figure 5(*a*) is taken 45.92 s and figure 5(*i*) 84.96 s after start-up. Therefore, figure 5(*a*) is extracted from the same full image as figure 4(*i*), so that the appearance of the cold intrusion, coincides with the passage of the hot intrusion past the mid-point of the cavity. The wave-like temperature structures of the nose discussed above are clearly visible. They remain present throughout the sequence, although decreasing in amplitude, presumably due to dispersion. The production of these wave-like structures obviously continues throughout the passage of the intrusion, with as many as five such temperature maxima visible in figure 5(*h*), taken at $t = 80.88$ s. The last image of this sequence (figure 5*i*) shows the impact of the intrusion on the bottom part of the heated boundary layer, which as a result changes its shape and dynamics in this region.

3.3. *Second group of travelling waves*

The effect of the impact of the cold intrusion on the base of the hot boundary layer is shown in figure 6. This time series is similar to figure 3 with each frame again showing the same vertical strip (≈ 1.1 cm wide) around the hot boundary layer. The time elapsed between consecutive pictures is 2.44 s with figure 6(*a*) taken 82.52 s and figure 6(*v*) 133.76 s after start-up. Therefore, figure 6(*b*) corresponds to the same full frame as figure 5(*i*). Figure 6(*a*) is taken prior to the impact, with the nose of the cold intrusion being just visible. Another feature which is evident from figure 6(*a*, *b*) is the fact that the intrusion head itself has thickened, compared for example to figure 5(*a*, *b*). Owing to the narrowness of the region shown in figure 5, this could not be viewed there. During impact, that part of the intrusion, over which it interacts with the boundary layer, widens as shown by the increased height of the disturbance at the bottom of the vertical boundary layer. This continues until figure 6(*g*) ($t = 94.72$ s) when it starts to slowly collapse back. As discussed below in § 4.3, this is consistent with the 'piling-up' of intrusion fluid as suggested by Patterson & Imberger (1980).

From the impact of the cold intrusion, which represents a strong disturbance of the (unstable) hot boundary layer, an instability in the form of waves travelling along this boundary layer is expected. This second group of waves can clearly be seen in figure 6. The first wave is most obvious in figure 6(*k*), but can already be observed in figure 6(*i*), taken at $t = 102.04$ s. It can then be followed up the boundary layer for the next three images before reaching the downstream corner by figure 6(*m*) at $t = 111.80$ s. The passage of five more wave peaks may be identified, with the last one disappearing by figure 6(*t*), taken at $t = 128.88$ s. In the last two frames (figure 6*u*, *v*) no sign of wave motion can be detected, and the cavity flow now very slowly approaches a steady state.

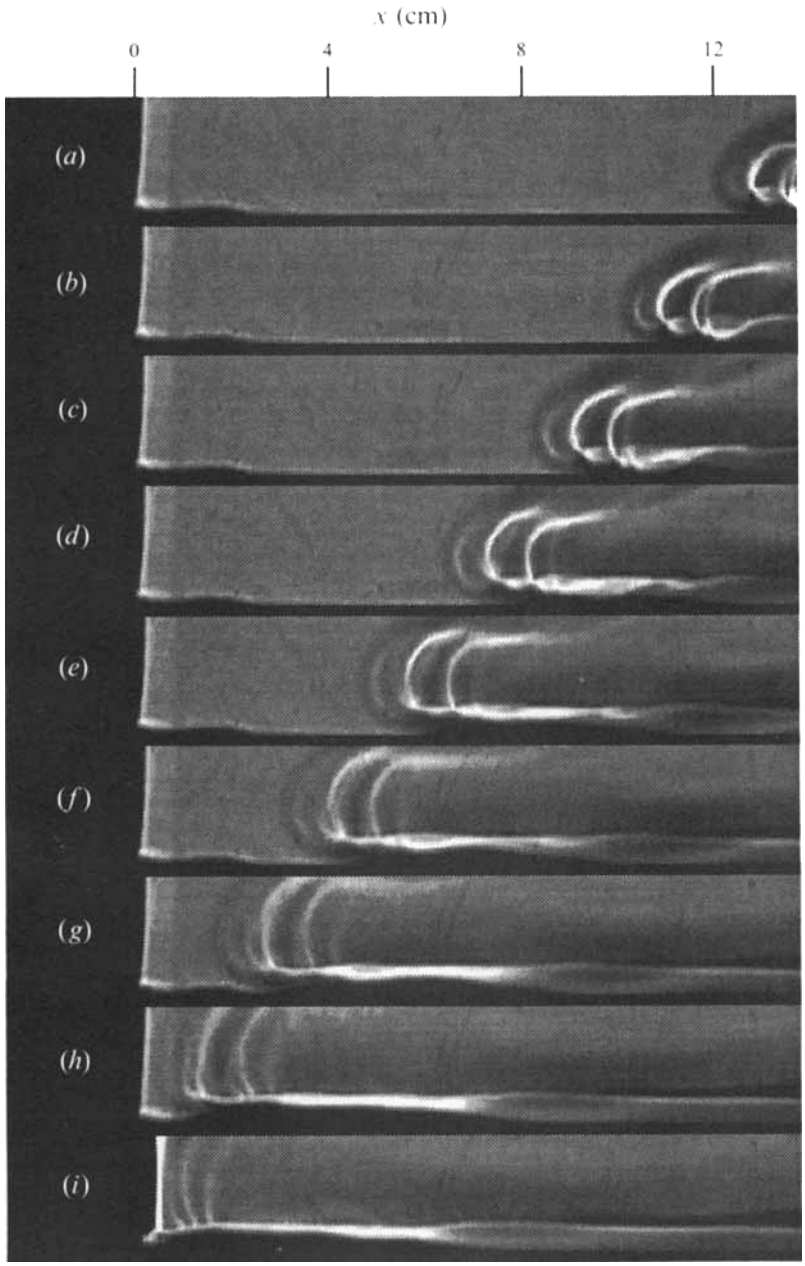

FIGURE 5. Time series of shadowgraph images showing the cold intrusion. The labels at the top indicate the distance in cm from the hot (left) wall. Similarly to figure 4, each part now represents the same region ($\approx$ 2.46 cm) of the tank around the bottom boundary, again with 4.88 s elapsed between consecutive images. The individual parts correspond to the following times after start-up: (*a*) 45.92 s, (*b*) 50.80 s, (*c*) 55.68 s, (*d*) 60.56 s, (*e*) 65.44 s, (*f*) 70.32 s, (*g*) 75.20 s, (*h*) 80.08 s, (*i*) 84.96 s. Several thermal features being shed by the nose can be distinguished and are discussed in the text.

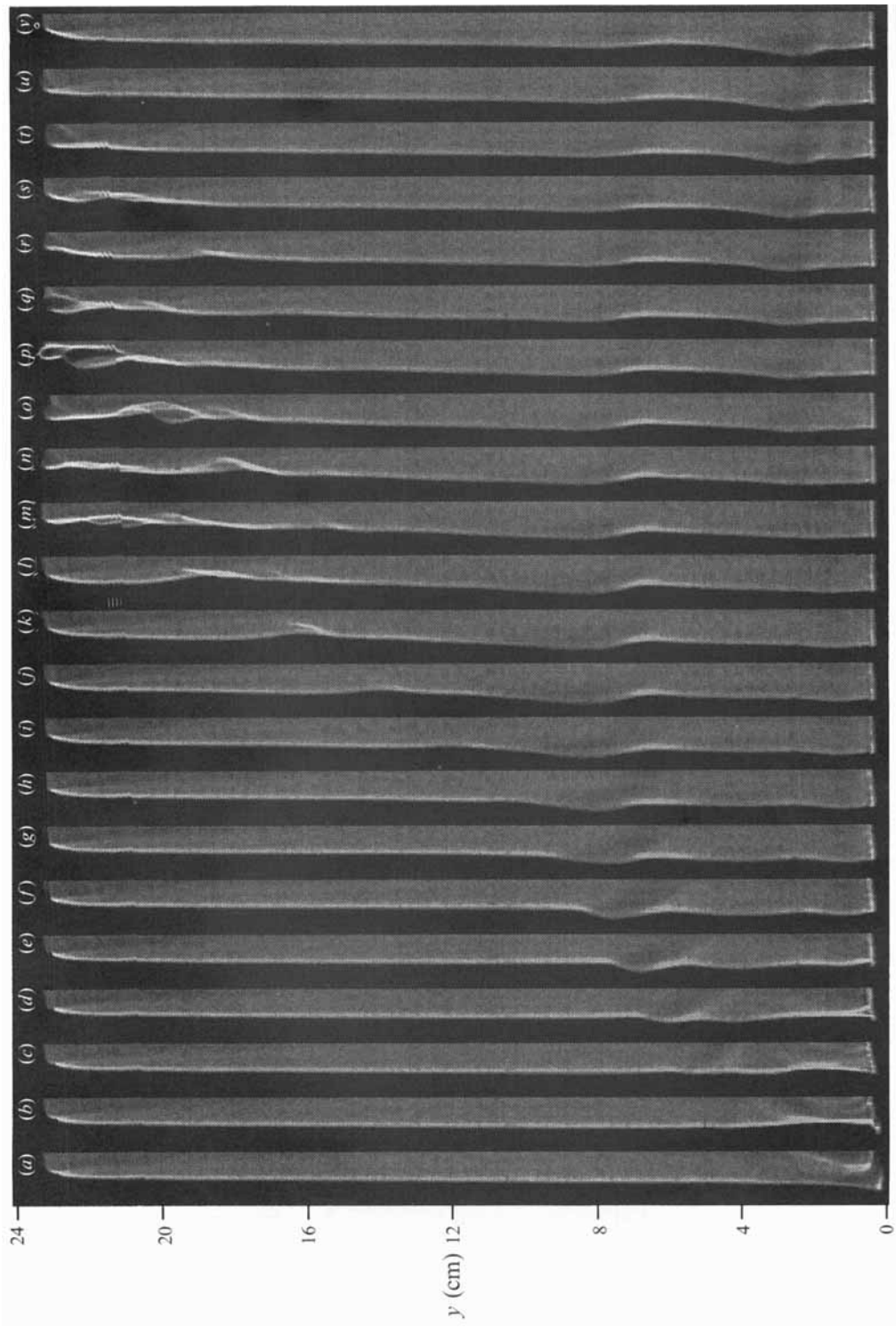

FIGURE 6. For caption see facing page.

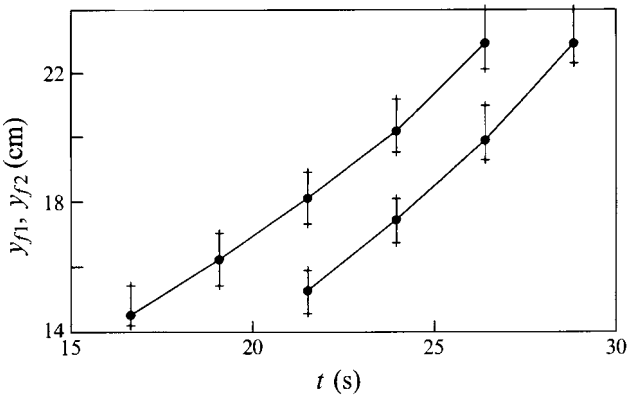

FIGURE 7. Motion of the first group of waves up the hot boundary layer as extracted from figure 3. The filled circles are the locations y_{f1} and y_{f2} of the centre points of the wave peaks plotted as a function of time t after start-up. The crosses indicate the extent of the respective peaks up and down the boundary layer and therefore they do not correspond to error bars in the usual sense. The upper curve represents the first (figure 3*d–h*) and the lower curve the second wave peak (figure 3*f–i*). The lines between the dots are only guides to the eye.

4. Results and discussion

4.1. *First group of travelling waves*

Figure 3 gives a clear indication of both the existence and the passage of a group of waves travelling up the hot boundary layer. These waves are associated with the start-up of the flow and are consistent with the observations reported by Schladow (1990), Patterson & Armfield (1990), Armfield & Patterson (1992) and Jeevaraj & Patterson (1992).

The locations y_{f1} and y_{f2} of the two wave peaks along the boundary layer can be estimated from figure 3 and are plotted as a function of time t after start-up in figure 7. Here, the filled circles correspond to the position of the white markers shown in figure 3, which identified the maximal deflection of the temperature signal (the 'brightest spot') at each available time. The crosses above and below each circle indicate the extent of the respective peak as well as it can be extracted from figure 3, and the bars are therefore not error bars in the usual sense. The lines connecting the circles are only guides to the eye. The left curve corresponds to the passage of the first peak and the right curve to the second peak. Although the data are limited, it is evident from both curves that the wave speed is not constant, but increases as the

FIGURE 6. Time series of shadowgraph images showing the second group of travelling waves. The labels at the left-hand side indicate the distance in cm from the bottom. Similarly to figure 3, each part again represents the same region ($\approx$ 1.1 cm) of the tank around the hot boundary layer with 2.44 s elapsed between consecutive images. The individual parts correspond to the following times after start-up: (*a*) 82.52 s, (*b*) 84.96 s, (*c*) 87.40 s, (*d*) 89.84 s, (*e*) 92.28 s, (*f*) 94.72 s, (*g*) 97.16 s, (*h*) 99.60 s, (*i*) 102.04 s, (*j*) 104.48 s, (*k*) 106.92 s, (*l*) 109.36 s, (*m*) 111.80 s, (*n*) 114.24 s, (*o*) 116.68 s, (*p*) 119.12 s, (*q*) 121.56 s, (*r*) 124.00 s, (*s*) 126.44 s, (*t*) 128.88 s, (*u*) 131.32 s, (*v*) 133.76 s. The piling-up of the intrusion as a consequence of its impact on the hot boundary layer can be seen from (*b–g*). The first sign of a wave can be identified in (*i*) just above this structure and then followed until its arrival at the top corner in (*m*). Five more peaks can be extracted from this picture with no further wave motion evident in (*u,v*).

waves travel up the boundary layer. This is consistent with the numerical results of Armfield & Patterson (1992).

A system which, at least for the early stages, behaves similarly to the one described here (see also beginning of § 3) is the start-up flow on a suddenly heated *semi-infinite* plate (see for example Goldstein & Briggs 1964; Ostrach 1964; Brown & Riley 1973). Following the initial heating, the flow at any position along the plate is at first governed by the one-dimensional boundary-layer solution appropriate for the *doubly infinite* plate, as described by Goldstein & Briggs (1964). However, the presence of the leading edge is felt after some time, and a transition to the two-dimensional steady flow described by Ostrach (1964) occurs. This transition is associated with a group of waves travelling up the boundary layer. The similarity between this flow and the initial flow adjacent to the wall in the differentially heated and cooled cavity was noted by Schladow (1990). It was suggested by Armfield & Patterson (1992) that the transition from one- to two-dimensional flow moves at the speed of the fastest travelling wave, which is greater than the maximal velocity of the fluid in the boundary layer. According to this, the waves are the result of the interaction of the leading-edge singularity with the unstable boundary layer, and a certain spectrum of waves is amplified as they travel up the wall.

Armfield & Patterson (1992) used a linear stability analysis to calculate the phase speed and amplification of these travelling waves as a function of the wavenumber. This analysis was performed by perturbing the numerically generated vertical velocity and temperature fields in the cavity flow, assuming that two-dimensional effects were small. The resulting wave speeds and wavenumbers were consistent with those observed in both the experiments and the numerical simulations. A stability analysis for the solution found by Goldstein & Briggs (1964) gave almost identical results, confirming the view that the boundary layer for the initial part of the flow in the cavity behaves essentially like the boundary-layer flow on a semi-infinite plate.

The stability analysis by Armfield & Patterson (1992) was done at a Rayleigh number of $\overline{Ra} = 6 \times 10^8$, which in their notation was based on the temperature difference between the hot and cold walls. In our scaling (temperature difference between the wall and the ambient) this corresponds to $Ra = 3 \times 10^8$, being lower by a factor of about two than the Rayleigh number used in our experiment. However, it may be shown that the stability equations can be written in terms of a single perturbation parameter (see for example Krane & Gebhart 1993). Their analysis was done for a constant-flux boundary condition rather than the constant-temperature condition relevant here, but an equivalent calculation for our situation reveals that the perturbation is governed by the product of Ra and $t^{3/2}$, for other parameters fixed (private communication by A.M.H. Brooker). Thus the results of Armfield & Patterson (1992) given at a certain time will correspond to an earlier time for the higher Rayleigh number case. The highest time they considered was $t = 27.1$ s for $Ra = 3 \times 10^8$, which translates into $t \approx 15$ s for $Ra = 7.2 \times 10^8$.

A quantitative comparison between the linear stability analysis of Armfield & Patterson (1992) and our experimental results is therefore possible. We can approximate the velocity of the waves from the data of figure 7 simply by assuming a constant speed between two data points, which yields an estimate for the velocity at intermediate times and locations. The velocities found in this way are given as functions of time in table 1. Our first indication of a wave is at $t = 16.64$ s (see figure 3*d*), therefore the first estimate of the velocity can be given at $t = 17.86$ s with 7 mm s^{-1}. According to the calculation by Armfield & Patterson (1992), the maximally amplified wave should travel with a phase speed of 5 mm s^{-1}, however at a time $t = 15$ s which is well

t (s)	v_{f1} (mm s^{-1})	v_{f2} (mm s^{-1})
17.86	7.0	—
20.30	7.8	—
22.74	8.5	8.9
25.18	11.3	10.1
27.62	—	12.4

TABLE 1. Velocities of the first (v_{f1}) and second (v_{f2}) peak of the first group of waves as a function of time t after start-up. The velocities are calculated from the data of figure 7 by assuming a constant speed between two data points.

before our earliest observation. A linear extrapolation of the data given in table 1 to $t = 15$ s yields a velocity of 6.1 mm s^{-1}, which is still a somewhat larger value. For those temporally coinciding observations, the second peak travels at approximately the same speed as the first one.

There are clearly insufficient data to draw any definite conclusion except that our observations are consistent with the stability calculations by Armfield & Patterson (1992). This suggests that the waves we see in the shadowgraph images represent in fact the maximally amplified component of a spectrum of waves, moving up the boundary layer with a phase velocity which is in reasonable agreement with the predictions of the stability analysis. For a better quantitative comparison, however, the stability data for later times and therefore more appropriate for our experiment would be desirable.

4.2. *Horizontal intrusions*

The development and progress of the initial horizontal intrusion of heated fluid as the hot boundary layer discharges into the cavity at the downstream corner is shown in figure 4 and, through symmetry with the cold intrusion, in figure 5. The motion of the respective intrusions is represented by figure 8. The crosses indicate the position x_{hn} of the nose of the hot intrusion as a function of time t after start-up, while the open circles correspond to the nose of the cold intrusion (x_{cn}). The small mismatch in locations at the mid-point of the cavity (12 cm) is due to the slight lack of symmetry as discussed earlier in § 2.3. The filled circles and the open and filled squares in figure 8 are the locations x_{c1}, x_{c2} and x_{c3} of the first three temperature structures of the cold intrusion as shown in figure 5 and discussed above in § 3.2. A weak dispersion of these temperature structures is evident.

Figure 9 shows the absolute values of the velocities for both intrusion noses as a function of the distance x from the hot wall, calculated in the same way as the velocities for the first group of waves above. The crosses correspond to the nose of the hot intrusion (v_{hn}) travelling to the right from 0 to 12 cm, and the open circles to the cold intrusion ($-v_{cn}$) travelling to the left from 12 to 0 cm. The two curves are approximately symmetric, indicating that the intrusion nose accelerates over the first half of the cavity, reaching a maximum velocity of about 4 mm s^{-1} half-way through the cavity, and then decelerates in the second half by about the same rate.

The intrusion structure is highly complex, with the interaction between the incoming waves from the boundary layer and the detraining fluid on the outer edge of the intrusion behind the head, and with evidence of an instability occurring at the nose. While there are some similarities between the early part of the intrusion and the usual form of a gravity current (see for example Britter & Simpson 1978; Simpson

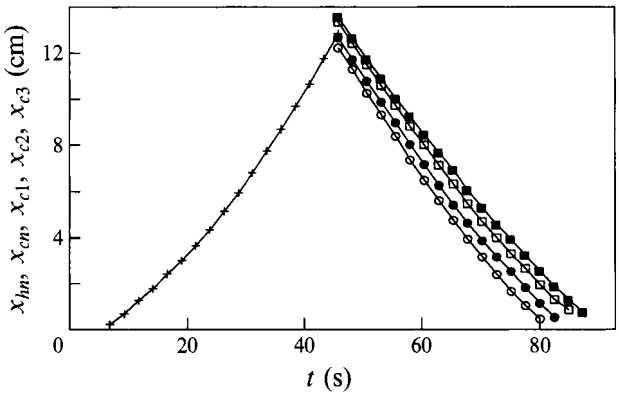

FIGURE 8. Motion of the top and bottom intrusions as extracted from figures 4 and 5. The crosses to the left and the open circles to the right represent the respective locations x_{hn} and x_{cn} of the hot and cold intrusion noses as functions of time t after start-up. The filled circles as well as the open and filled squares correspond to the locations x_{c1}, x_{c2} and x_{c3} of the first three thermal features inside the cold intrusion head, as shown in figure 5. Again, the lines are only guides to the eye.

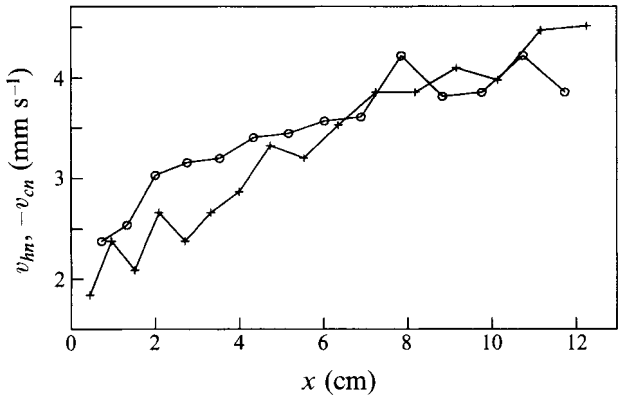

FIGURE 9. Velocities of the hot and cold intrusion noses as functions of the distance x from the hot wall. The velocities are calculated from the data of figure 8 by assuming a constant speed between two data points. The crosses correspond to the hot (v_{hn}) and the open circles to the cold intrusion nose ($-v_{cn}$), indicating that the motion is approximately symmetric. The lines merely connect the individual measurement points.

& Britter 1979; Simpson 1982), there are also major differences especially in the later stages. This is not surprising since most of the experiments involving gravity currents are carried out at relatively large values of the Reynolds number $Re = ul/\nu$ of the order of 1000 or more. Here, u is the velocity and l the lateral dimension of the current. Estimating for our experiments the intrusion velocity as 4 mm s^{-1} and the thickness of the flow as 2 cm yields $Re = O(80)$, which is much smaller than the values in the experiments mentioned above. From figure 4, no turbulent mixing of the detraining fluid behind the head is evident.

One feature in particular which makes the intrusion in our case unique compared to gravity currents is the presence of the incoming waves from the hot boundary layer. They disrupt the intrusion structure and form a well-defined oscillatory modulation of the temperature signal in the part of the flow following directly behind the head,

as can be seen from figure 4(*f–j*). The waves appear to become trapped by the detraining structure and form bands of temperature features in the outer half of the following flow. At the same time, but independently, the intrusion head seems to be unstable, and wave-like structures, which subsequently travel together with the head, are formed behind the nose, as shown in figure 4(*f–h*) and throughout figure 5.

In the experiments by Patterson & Armfield (1990) and Jeevaraj & Patterson (1992), waves have been observed in the temperature signals of the horizontal intrusion flow, and it was assumed that these are the remnants of the incoming boundary-layer waves. Unfortunately, no simultaneous flow visualization was done in those experiments. On the other hand, our present results suggest that those previous observations correspond to the temperature structures shed by the nose. This is supported by the fact that the temperature modulations coming from the boundary-layer waves disperse relatively quickly during the passage of the intrusion (see figure 4*f–k*). They are no longer present in the second half of the passage, as can be seen in figure 5 for the data of the cold intrusion coming from the far wall, while Patterson & Armfield (1990) and Jeevaraj & Patterson (1992) still measured temperature oscillations in this later stage of the intrusion flow. From figures 4 and 5 it is clear that the waves present in this stage of the intrusion flow are the ones being shed by the intrusion nose.

Another interesting feature which distinguishes this intrusion flow from the usual gravity currents is the presence of a temperature structure near the top wall, first visible in figure 4(*e*) at about the mid-point of the intrusion length. This structure slowly moves out as the intrusion proceeds (figure 4*f–j*) and is consistent with the flow separation observed numerically and experimentally by Patterson & Armfield (1990). These authors suggested that the rapid divergence was due to the stratified nature of the intrusion itself. Coming from the hot boundary layer, the vertical temperature gradient of the horizontal intrusion is not zero at the top boundary, while the insulating boundary condition forces a vanishing gradient there. As a result, the intrusion flow has to adjust to this new boundary condition which may lead to a separation of the flow from the boundary. Other explanations for the nature of this flow structure include the hypothesis of an internal hydraulic jump (see for example Ivey 1984) and a mechanism which likened the behaviour to the discharge from a thermal plume (Ravi *et al.* 1994). From a calculation of the dissipated energy, this latter work showed that the structure is not consistent with a hydraulic jump. However, the thermal plume model was based on the assumption of a stratified ambient fluid and would therefore be more relevant to the flow structure much later in the development. Since the mechanism of interest is obviously responsible for the separation at the early as well as the later stages of the flow evolution, it seems that this latter model also is not appropriate. It is not clear which, if any, of the discussed mechanisms is responsible for the behaviour, but it is clear that the separation from the wall plays an important role in the dynamics of the intrusion.

4.3. *Second group of travelling waves*

The behaviour of the hot boundary layer after the impact of the cold intrusion is demonstrated by figure 6. The first five images after impact (figure 6*c–g*) clearly show the 'piling-up' of cold water against the boundary layer, as described by Patterson & Imberger (1980) and Patterson & Armfield (1990). This mechanism is based on the balance between the total entrainment from the cavity core into the boundary layer and the discharge from the boundary layer into the horizontal intrusion. Since the boundary layer is entraining over its full length but the intrusion interaction is over a much shorter distance, the boundary layer cannot accept all of the incoming

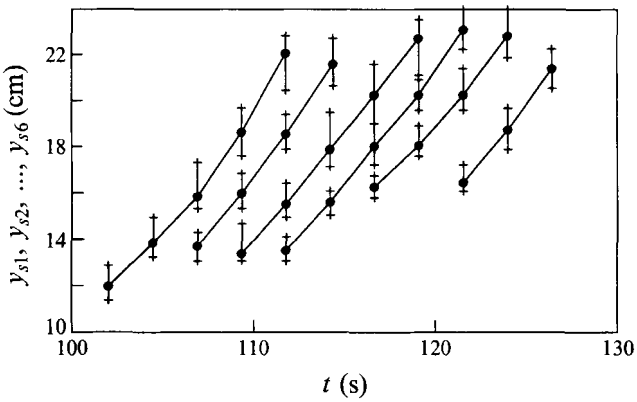

FIGURE 10. Motion of the second group of waves up the hot boundary layer as extracted from figure 6. The representation is analogous to figure 7 with the filled circles showing the locations $y_{s1}, y_{s2}, \ldots, y_{s6}$ of the centre points of the wave peaks as functions of time t after start-up and the crosses their extent along the boundary layer. The left-most curve corresponds to the first and the right-most curve to the sixth wave peak. Again, the lines are only guides to the eye.

fluid which consequently 'piles up' before relaxing back in a complex gravitational adjustment, as described by Patterson & Armfield (1990). The boundary layer itself is unstable, and the disturbance by the incoming intrusion has triggered another group of waves which subsequently travel up the layer. They are obvious from figure 6(*i*) throughout the series to figure 6(*t*), and six separate wave peaks may be identified. The position of each of these peaks is shown in figure 10 as a function of time t after start-up, plotted in the same format as for the first group of waves in figure 7. Again, the velocities increase during the passage up the boundary layer.

The stability analysis by Armfield & Patterson (1992) was performed for the transient boundary layer, while the second group of waves travel on an almost steady, fully developed boundary layer, although still in a non-stratified ambient. Armfield (1993) has reported some preliminary results of the required stability analysis for the steady boundary layer. This was done, however, for a stratified cavity core and for a Rayleigh number of $Ra = 3\times10^8$, which is much lower than the one in our experiment. He obtained a velocity of 3.5 mm s^{-1} for the maximally amplified wave at the mid-height of the cavity (12 cm). Owing to the large difference in Rayleigh numbers and the different internal stratification, no conclusion can be drawn from a comparison of this value with the velocity of 7.8 mm s^{-1} observed in our measurements at a height of 13 cm. A linear stability analysis using the more appropriate solution described by Ostrach (1964) as the base flow in an otherwise non-stratified fluid has been carried out by Brooker (1993). We will compare his results with our experiments below.

Figure 11 shows the velocities of the individual peaks of the travelling waves as functions of the height y above the bottom corner. Figure 11(*a*) corresponds to the second group of waves. It is evident that the velocities $v_{s1}, v_{s2}, \ldots, v_{s6}$ of each of these peaks are in general of about the same order and show the same trend as a function of position. This is consistent with the view that the properties of the amplified spectrum are the same for each individual wave. The open and filled circles correspond to the first and second wave peak, the open and filled squares to the third and fourth, and the open and filled triangles to the fifth and sixth peak. The thick line extending over the whole of the figure results from the stability analysis by Brooker (1993) mentioned in the previous paragraph, and obviously describes the trend very well. The velocities

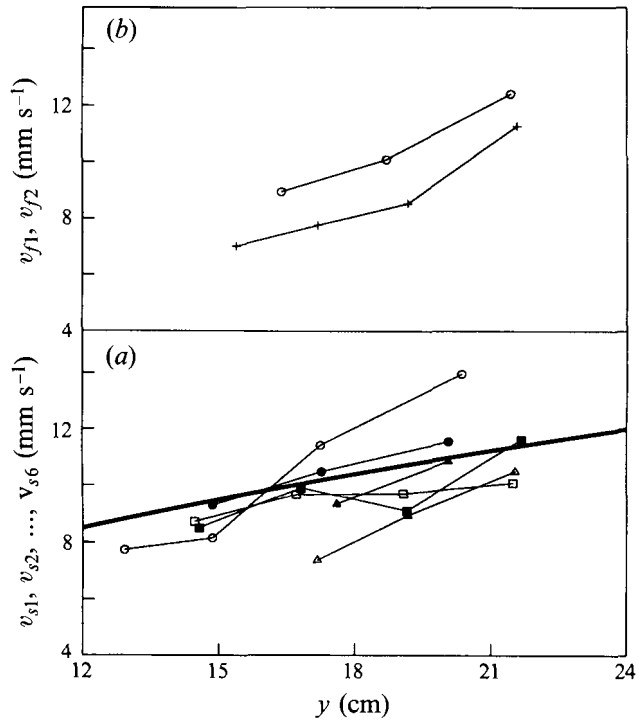

FIGURE 11. Velocities of the first and second groups of waves as functions of the distance y from the lower corner. The velocities are calculated from the data of figures 7 and 10 by assuming a constant speed between two data points. (*a*) The velocities $v_{s1}, v_{s2}, \ldots, v_{s6}$ for the second group of waves are shown, where peaks one to six are represented by the open and filled circles, open and filled squares, and the open and filled triangles, respectively. The thick line is the result of a linear stability analysis by Brooker (1993). (*b*) The velocities v_{f1} and v_{f2} for the first group of waves are shown with the crosses corresponding to the first peak and the circles to the second one. Again, all lines are merely connections between the individual data points belonging to the same wave.

for the first group of waves are given in figure 11(*b*) with the crosses corresponding to the first (v_{f1}) and the circles to the second wave peak (v_{f2}). They show a similar behaviour and are of about the same order as those of the second group of waves, thus indicating that despite the differences of the boundary layers in both cases, they are similar with respect to travelling waves.

5. Conclusions and outlook

For the flow in a differentially heated and cooled cavity, several sequences of shadowgraph images have been used to visualize for the first time the two wave groups travelling on the vertical boundary layer, the first one following initiation and the second one the impact of the incoming intrusion from the far wall. The properties of these waves have been shown to be consistent with earlier experimental and numerical observations, albeit at different Rayleigh numbers. Further, the properties of the first intrusion have been displayed in a new way, identifying the formation of waves at the nose of the intrusion, the interaction of the incoming boundary-layer waves with the detraining fluid behind the intrusion head, and the formation of a separation zone against the wall. These features distinguish this stratified intrusion

from a usually homogeneous gravity current, although it displays some of the features of the latter.

The observations reported in this paper represent the first in a series of experiments directed at providing the details of the boundary-layer properties following start-up and the impact of the incoming intrusion as well as the subsequent evolution to a steady state. These observations must now be coupled with a study of the stability of both the growing boundary-layer perturbed by the initial start-up, with reference to the first group of waves, and the steady boundary layer perturbed by the impact of the incoming intrusion, with reference to the second group of waves. These stability studies are currently under way and will be reported separately.

Likewise, the observation of the first intrusion has revealed a number of features of the flow which have not previously been noted. In particular, the apparent instability of the intrusion nose and the trapping of the incoming boundary-layer waves lead to two distinct temperature structures inside the intrusion, which is quite different to what has been proposed previously. No mechanism has been suggested yet for these complex interactions. The formation of the separation zone between the intrusion and the horizontal wall also requires a description, although some mechanisms have been proposed for this structure. These are, however, in the context of the steady flow rather than the first intrusion and are not complete in any sense. Experiments which look in more detail at the intrusion flow at different Rayleigh numbers and which also cover the evolution to the subsequent steady state are currently under preparation.

Useful discussions with Steve Armfield and Andrew Brooker are gratefully acknowledged. This research was supported by the Australian Research Council under grants A89231072 and A89331991. W.S. is the recipient of a University Postdoctoral Research Fellowship by the University of Western Australia.

REFERENCES

ARMFIELD, S. W. 1993 Boundary layer instabilities in steady state cavity convection flow. *Proc. Fourth Australian Natural Convection Workshop, Perth, December 1–3. Rep.* ED 834. Centre for Water Research, University of Western Australia.

ARMFIELD, S. W. & PATTERSON, J. C. 1992 Wave properties of natural-convection boundary layers. *J. Fluid Mech.* **239**, 195–211.

BRIGGS, D. G. & JONES, D. N. 1985 Two-dimensional periodic natural convection in a rectangular enclosure of aspect ratio one. *Trans. ASME C: J. Heat Transfer* **107**, 850–854.

BRITTER, R. E. & SIMPSON, J. E. 1978 Experiments on the dynamics of a gravity current head. *J. Fluid Mech.* **88**, 223–240.

BROOKER, A. M. H. 1993 The properties of transient instabilities in a boundary layer. *Proc. Fourth Australian Natural Convection Workshop, Perth, December 1–3. Rep.* ED 834. Centre for Water Research, University of Western Australia.

BROWN, S. N. & RILEY, N. 1973 Flow past a suddenly heated vertical plate. *J. Fluid Mech.* **59**, 225–237.

BUSSE, F. H. & WHITEHEAD, J. A. 1971 Instabilities of convection rolls in a high Prandtl number fluid. *J. Fluid Mech.* **47**, 305–320.

GOLDSTEIN, R. J. & BRIGGS, D. G. 1964 Transient free convection about vertical plates and circular cylinders. *Trans. ASME C: J. Heat Transfer* **86**, 490–500.

HENKES, R. A. W. M. & HOOGENDOORN, C. J. 1990 On the stability of natural-convection flow in a cavity heated from the side. *Appl. Sci. Res.* **47**, 195–220.

INGHAM, D. B. 1985 Flow past a suddenly heated vertical plate. *Proc. R. Soc. Lond.* A **402**, 109–134.

IVEY, G. N. 1984 Experiments on transient natural convection in a cavity. *J. Fluid Mech.* **144**, 389–401.

JANSSEN, R. J. A., HENKES, R. A. W. M. & HOOGENDOORN, C. J. 1993 Transition to time-periodicity of a natural-convection flow in a 3D differentially heated cavity. *Intl J. Heat Mass Transfer* **36**, 2927–2940.

JEEVARAJ, C. G. & PATTERSON, J. C. 1992 Experimental study of transient natural convection of glycerol–water mixtures in a side heated cavity. *Intl J. Heat Mass Transfer* **35**, 1573–1587.

JOSHI, Y. & GEBHART, B. 1987 Transition of transient vertical natural-convection flows in water. *J. Fluid Mech.* **179**, 407–438.

KRANE, M. J. M. & GEBHART, B. 1993 The hydrodynamic stability of a one-dimensional transient buoyancy-induced flow. *Intl J. Heat Mass Transfer* **36**, 977–988.

LE QUÉRÉ, P. 1990*a* A note on multiple and unsteady solutions in two-dimensional convection in a tall cavity. *Trans. ASME C: J. Heat Transfer* **112**, 965–974.

LE QUÉRÉ, P. 1990*b* Transition to unsteady natural convection in a tall water-filled cavity. *Phys. Fluids* A **2**, 503–515.

LE QUÉRÉ, P. & PENOT, F. 1987 Numerical and experimental investigation of the transition to unsteady natural convection of air in a vertical differentially heated cavity. *ASME Heat Transfer Div.* **94**, 75–82.

MERZKIRCH, W. 1974 *Flow Visualization*. Academic.

OSTRACH, S. 1964 Laminar flows with body forces. In *Theory of laminar flows* (ed. F. K. Moore), pp. 528–718. Princeton University Press.

PAOLUCCI, S. & CHENOWETH, D. R. 1989 Transition to chaos in a differentially heated cavity. *J. Fluid Mech.* **201**, 379–410.

PATTERSON, J. C. & ARMFIELD, S. W. 1990 Transient features of natural convection in a cavity. *J. Fluid Mech.* **219**, 469–497.

PATTERSON, J. & IMBERGER, J. 1980 Unsteady natural convection in a rectangular cavity. *J. Fluid Mech.* **100**, 65–86.

RASENAT, S., HARTUNG, G., WINKLER, B. L. & REHBERG, I. 1989 The shadowgraph method in convection experiments. *Exps. Fluids* **7**, 412–419.

RAVI, M. R., HENKES, R. A. W. M. & HOOGENDOORN, C. J. 1994 On the high-Rayleigh-number structure of steady laminar natural-convection flow in a square enclosure. *J. Fluid Mech.* **262**, 325–351.

SCHLADOW, S. G. 1990 Oscillatory motion in a side-heated cavity. *J. Fluid Mech.* **213**, 589–610.

SCHLADOW, S. G., PATTERSON, J. C. & STREET, R. L. 1989 Transient flow in a side-heated cavity at high Rayleigh number: a numerical study. *J. Fluid Mech.* **200**, 121–148.

SCHÖPF, W. & REHBERG, I. 1994 The influence of thermal noise on the onset of travelling-wave convection in binary fluid mixtures: an experimental investigation. *J. Fluid Mech.* **271**, 235–265.

SIMPSON, J. E. 1982 Gravity currents in the laboratory, atmosphere, and ocean. *Ann. Rev. Fluid Mech.* **14**, 213–234.

SIMPSON, J. E. & BRITTER, R. E. 1979 The dynamics of the head of a gravity current advancing over a horizontal surface. *J. Fluid Mech.* **94**, 477–495.

WINKLER, B. L. & KOLODNER, P. 1992 Measurements of the concentration field in nonlinear travelling-wave convection. *J. Fluid Mech.* **240**, 31–58.

YEWELL, R., POULIKAKOS, D. & BEJAN, A. 1982 Transient natural convection experiments in shallow enclosures. *Trans. ASME C: J. Heat Transfer* **104**, 533–538.